

Coupled Analysis of Independently Modeled Finite Element Substructures by Moving Least Squares Displacement Welding Technique

Jin Yeon Cho¹, Jae Mo An², You Me Song¹, Seungsoo Lee¹ and Dong Whan Choi¹

Abstract: A displacement welding technique is proposed to carry out coupled analysis of the integrated whole model which consists of independently modeled finite element substructures. In the proposed method, the incompatible displacement fields in the interfaces of independently modeled substructures are directly welded together through a blended function that is newly defined in the transient region of mismatching interface. To construct the blended function, the moving least squares function, which does not require well-defined nodal connectivity, is utilized along with the original finite element shape function. The meshless character of the moving least squares function makes it possible to efficiently handle the mismatching interfaces of independently modeled finite element substructures. To prove the validity of the proposed method, the patch tests and convergence tests are carried out for various mismatching models. To assess the performance of the proposed welding technique, several numerical examples are worked out including beam type problem, plate with circular hole, and L-shaped beam type problem. As a practical application, example of three dimensional coupled analysis of independently modeled substructures is presented.

keyword: Displacement Welding Technique, Mismatching Interface, Transient Region, Moving Least Squares Function.

1 Introduction

Complex structural systems, such as aircrafts, spacecrafts, automobiles, are usually modeled collaboratively in the form of substructures, and the substructures or subparts are modeled independently by several engineers. Thus, generally the independently modeled finite element substructures do not satisfy the nodal compati-

bility in the interfaces of each substructure. And the nodal incompatibility makes it difficult to carry out the coupled analysis of the integrated whole model. Due to the reason, considerable attention has been given to the coupled analysis of independently modeled finite element substructures during the past decade [Ransom, McCleary, Aminpour (1993); Aminpour, Ransom, McCleary (1995); Farhat and Mandel (1998); Park and Felippa, (2000); Aminpour, Pageau, Shin (2001)].

Of course, one easiest remedy may be the design of transition elements in the interface region of independently modeled substructures [Bathe (1996); Kim (2002)]. However, this approach is somewhat cumbersome to apply and may need expensive human labor in practical situations because there are various cases and combinations to be considered. Therefore, different approaches have been explored to solve the trouble. Of these, one major approach is the introduction of Lagrange multiplier in the interface region to satisfy both of the displacement compatibility and force equilibrium in variational sense [Aminpour, Pageau, and Shin (2001)]. The approach is more flexible to handle the independently modeled finite element substructures than the transition element, and in mathematical sense the nodal compatibility is no longer required in the interface region. However this Lagrange multiplier approach necessarily requires the additional unknowns, and does not preserve the positive definiteness and banded structure of stiffness matrix of the whole coupled system. Also it frequently needs some additional interface meshes to appropriately enforce the constraint conditions of displacement compatibility.

Therefore, in this work a novel approach, where the incompatible displacement fields of independently modeled substructures are directly welded together, is proposed to efficiently carry out the coupled analysis of independently modeled finite element substructures without introducing any additional unknown or any remeshing. Also, in the proposed method the positive definite-

¹ Department of Aerospace Engineering, INHA University, Korea

² Department of Aerospace Engineering, INHA University, Korea
Currently, Korea Aerospace Research Institute

ness and banded structures of the system stiffness matrix are no longer sacrificed because displacement fields of the independently modeled finite element substructures are directly welded into a compatible displacement field for whole coupled model. In displacement welding, moving least squares function [Lancaster and Salkauskas(1981); Nayroles, Touzot, and Villon (1992); Li, Shen, Han, and Atluri (2003)], which does not require any fixed nodal connectivity, is utilized along with the original finite element shape functions. In the next section, the moving least squares method is briefly reviewed.

2 Moving Least Squares Method

The moving least squares method is one of the most popular approximation schemes (along with Shepard function [Shepard (1968)], RKPM [Liu, Jun, and Chang (1995)], PUM [Babuska and Melenk (1997)], etc.) which does not need any element information. And for the most part, it is equivalent to the Shepard function, RKPM, and PU [Atluri and Shen (2002); Atluri (2004)]. The required smoothness of approximation function can be easily achieved by the moving least squares method. Due to these reasons, the moving least squares technique may give a good way to weld the displacement fields near the mismatching interfaces between the substructures with no regard to the nodal positions. In this section, the basic idea of the moving least squares approximation is briefly reviewed.

Consider a continuous function u defined on a domain Ω , where the (fictitious) nodal values at the scattered points \mathbf{x}_i ($1 \leq i \leq n$) in Ω , that enter the interpolation, are given as \hat{u}^i . To approximate the distribution of function u in Ω , the global approximation form $u^h(\mathbf{x})$ for $u(\mathbf{x})$ is defined as follows.

$$\text{For all } \mathbf{x} \in \Omega, u^h(\mathbf{x}) = \mathbf{p}^T(\mathbf{x})\mathbf{a}(\mathbf{x}) = \sum_{i=1}^m p_i(\mathbf{x})a_i(\mathbf{x}) \quad (1)$$

where $\mathbf{p}^T(\mathbf{x}) = [p_1(\mathbf{x}), p_2(\mathbf{x}), \dots, p_m(\mathbf{x})]$ is a monomial basis satisfying the conditions as

- (i) $p_1(\mathbf{x}) = 1$
- (ii) $p_i(\mathbf{x}) \in C^r(\Omega)$, $i = 1, \dots, m$
- (iii) There exists $\{\tilde{\mathbf{x}}_1, \dots, \tilde{\mathbf{x}}_m\} \subset \{\mathbf{x}_1, \dots, \mathbf{x}_n\}$ such that $\{\mathbf{p}(\tilde{\mathbf{x}}_1), \dots, \mathbf{p}(\tilde{\mathbf{x}}_m)\}$ is a linearly independent set.

where, $C^r(\Omega)$ denotes the set of functions, whose derivatives are continuous up to the r -th degree. For example,

the $(m-1)$ -th order monomial basis in one dimension has the following form:

$$\mathbf{p}^T(x) = [1, x, x^2, \dots, x^{m-1}] \quad (2)$$

In two dimension, a quadratic monomial basis is written as

$$\mathbf{p}^T(\mathbf{x}) = [1, x, y, x^2, xy, y^2] \quad (3)$$

Additionally, the paper [Atluri and Zhu (1998)] can be referred to, for other forms of monomial bases in two and three dimensional problems.

The vector $\mathbf{a}(\mathbf{x}) = [a_1(\mathbf{x}), a_2(\mathbf{x}), \dots, a_m(\mathbf{x})]^T$ is a vector of undetermined coefficients, whose values can vary according to the position $\mathbf{x} \in \Omega$. The coefficient vector $\mathbf{a}(\bar{\mathbf{x}})$ at each position $\mathbf{x} = \bar{\mathbf{x}}$ will be determined by a local weighted least squares approximation $u_{\bar{\mathbf{x}}}(\mathbf{x})$ of the function $u(\mathbf{x})$, in a sufficiently small neighborhood $nb\delta(\bar{\mathbf{x}})$ of $\mathbf{x} = \bar{\mathbf{x}}$.

A local approximation $u_{\bar{\mathbf{x}}}(\mathbf{x})$, for each point $\bar{\mathbf{x}} \in \Omega$, is defined as

$$u(\mathbf{x}) \cong u_{\bar{\mathbf{x}}}(\mathbf{x}) = \mathbf{p}^T(\mathbf{x})\mathbf{a}(\bar{\mathbf{x}}), \text{ for all } \mathbf{x} \in nb\delta(\bar{\mathbf{x}}) \quad (4)$$

In order that the local approximation is the best approximation to u in a certain least squares sense, the coefficient vector $\mathbf{a}(\bar{\mathbf{x}})$ is selected as the $m \times 1$ vector that minimizes the following weighted least squares discrete L_2 error norm.

$$\begin{aligned} J_{\bar{\mathbf{x}}}(\mathbf{b}) &= \sum_{i=1}^n w_i(\bar{\mathbf{x}}) [\mathbf{p}^T(\mathbf{x}_i)\mathbf{b} - \hat{u}^i]^2 \\ &= [\mathbf{P}\mathbf{b} - \hat{\mathbf{u}}]^T \mathbf{w}(\bar{\mathbf{x}}) [\mathbf{P}\mathbf{b} - \hat{\mathbf{u}}] \end{aligned} \quad (5)$$

That is, the coefficient vector $\mathbf{a}(\bar{\mathbf{x}})$ is selected to satisfy the following condition.

$$J_{\bar{\mathbf{x}}}(\mathbf{a}(\bar{\mathbf{x}})) \leq J_{\bar{\mathbf{x}}}(\mathbf{b}), \text{ for all } \mathbf{b} \in R^m \quad (6)$$

In Eq. (5), $w_i(\mathbf{x})$ is the weight function associated with the position \mathbf{x}_i of node i , and $w_i(\mathbf{x})$ is greater than 0 for all \mathbf{x} in the support domain (i.e., the region of non-zero values) of $w_i(\mathbf{x})$, and n denotes the number of nodes. For example, the support domain of the weight function $w_i(\mathbf{x})$ can be taken to be a sphere in 3-D; and the weight function $w_i(\mathbf{x})$ centered at each node \mathbf{x}_i is usually adopted to be positive and non-zero if the distance between node \mathbf{x}_i

and \mathbf{x} is less than a specified radius R_i , and to be zero if the distance is greater than or equal to the radius R_i , in order to preserve the local character of the MLS approximation.

The matrix \mathbf{P} is an $n \times m$ matrix, and $\mathbf{w}(\bar{\mathbf{x}})$ is $n \times n$ diagonal matrix written as follows.

$$\mathbf{P} = [\mathbf{p}(\mathbf{x}_1), \mathbf{p}(\mathbf{x}_2), \dots, \mathbf{p}(\mathbf{x}_n)]^T \quad (7)$$

$$\mathbf{w}(\bar{\mathbf{x}}) = \begin{bmatrix} w_1(\bar{\mathbf{x}}) & 0 & \dots & 0 \\ 0 & w_2(\bar{\mathbf{x}}) & \dots & \vdots \\ \vdots & \vdots & \ddots & 0 \\ 0 & \dots & 0 & w_n(\bar{\mathbf{x}}) \end{bmatrix} \quad (8)$$

And the vector $\hat{\mathbf{u}}$ denotes the vector of given fictitious values \hat{u}^i of variable u at nodes i ($1 \leq i \leq n$) as follows.

$$\hat{\mathbf{u}}^T = [\hat{u}^1, \hat{u}^2, \dots, \hat{u}^n] = [u(\mathbf{x}_1), u(\mathbf{x}_2), \dots, u(\mathbf{x}_n)] \quad (9)$$

It is noted that the \hat{u}^i ($1 \leq i \leq n$) are not the nodal values of the approximation function $u^h(\mathbf{x})$.

The method to approximate the function by the moving least squares method is sketched in Fig. 1. At each position $\mathbf{x} = \bar{\mathbf{x}}$, a local weighted least squares approximation is found by using Eqs. (4), (5) and (6), and its coefficient vector $\mathbf{a}(\bar{\mathbf{x}})$ is used in the global approximation form (1). Actually, it is the same as the moving procedure of local approximation to obtain the global approximation, as stated in the previous work [Lancaster and Salkauskas (1981)].

By applying the stationarity condition to the weighted discrete error norm, the coefficient vector $\mathbf{a}(\bar{\mathbf{x}})$ can be

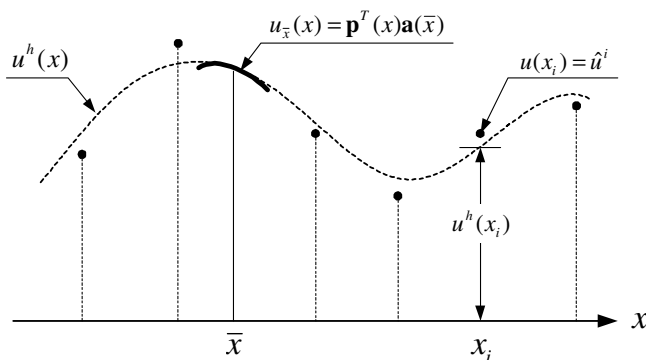


Figure 1 : Conceptual explanation of the moving least squares interpolation scheme

obtained from the following matrix equation.

$$\mathbf{A}(\bar{\mathbf{x}})\mathbf{a}(\bar{\mathbf{x}}) = \mathbf{B}(\bar{\mathbf{x}})\hat{\mathbf{u}} \quad (10)$$

where,

$$\begin{aligned} \mathbf{A}(\bar{\mathbf{x}}) &= \mathbf{P}^T \mathbf{w}(\bar{\mathbf{x}}) \mathbf{P} \\ \mathbf{B}(\bar{\mathbf{x}}) &= \mathbf{P}^T \mathbf{w}(\bar{\mathbf{x}}) \end{aligned} \quad (11)$$

Solving Eq. (10) for $\mathbf{a}(\bar{\mathbf{x}})$, and substituting it into Eq.(1) at $\mathbf{x} = \bar{\mathbf{x}}$, gives a relation which may be written in the form of a linear combination of nodal shape functions similar to that used in finite element method, as

$$u^h(\mathbf{x}) = \Psi^T(\mathbf{x})\hat{\mathbf{u}} = \sum_{i=1}^n \hat{u}^i \psi_i(\mathbf{x}) \quad (12)$$

where

$$\begin{aligned} \Psi^T(\mathbf{x}) &= \mathbf{p}^T(\mathbf{x})\mathbf{A}^{-1}(\mathbf{x})\mathbf{B}(\mathbf{x}) \\ \psi_i(\mathbf{x}) &= \sum_{j=1}^m p_j(\mathbf{x}) [\mathbf{A}^{-1}(\mathbf{x})\mathbf{B}(\mathbf{x})]_{ji} \end{aligned} \quad (13)$$

In actual computations, various kinds of weight functions can be adopted for MLS approximation procedure. The required condition for the continuity of the approximating function can be easily satisfied by changing the weight function in the MLS approximation procedure. In this work, we restrict ourselves to the twice differentiable weight function that has the form of

$$w_i(\mathbf{x}) = \begin{cases} 1 - 6 \left(\frac{d_i}{r_i}\right)^2 + 8 \left(\frac{d_i}{r_i}\right)^3 - 3 \left(\frac{d_i}{r_i}\right)^4, & \text{if } 0 \leq d_i \leq r_i \\ 0, & \text{if } d_i > r_i \end{cases} \quad (14)$$

where r_i denotes the radius of support of weight function and d_i denotes the distance between the point \mathbf{x} and nodal point \mathbf{x}_i . If the derivatives of monomial basis in the MLS approximation are continuous up to the r -th derivative, the resulting MLS approximation function from this weight function is continuously differentiable up to the minimum of 2 and r . One can also use other kinds of weight functions such as Gaussian weight function [Alturi and Shen (2002)].

3 Displacement Welding Procedure

3.1 Terminology

Let us consider non-overlapping independently modeled substructures which do not satisfy the nodal compatibilities in the interfaces of each substructure as shown in

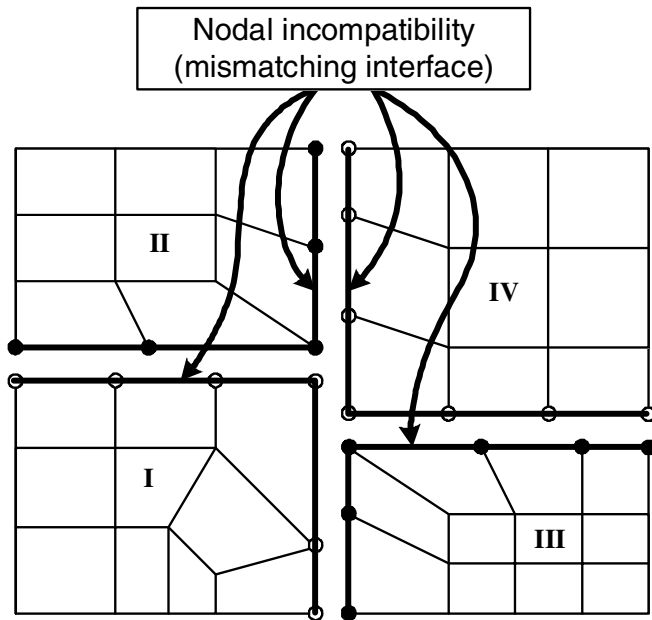


Figure 2 : Independently modeled substructures and mismatching interface

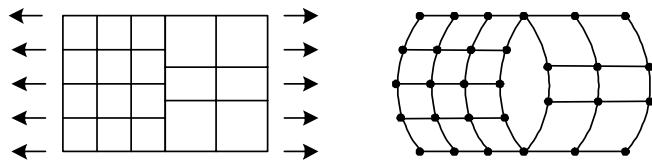


Figure 3 : Failure of coupled analysis induced by the incompatible displacement fields on mismatching interface

Fig. 2. If the substructures are assembled with no special treatment, then the displacement field on the interface of each substructure may become discontinuous, and as a result coupled analysis of the whole model may not be performed successfully as shown in Fig. 3.

To solve the trouble, a novel displacement welding technique is proposed in this work. For clear explanation of the proposed procedure, the following terminologies are used in this work. Firstly, common edge set for each finite element edge $\Gamma_\alpha^{(e)}$ (the α -th edge of e -th element) inside the domain is defined by the edge of which interior has a nonempty intersection with the interior of the considered finite element edge $\Gamma_\alpha^{(e)}$. Common edge set can be written in mathematical form as follows.

$$C_\alpha^{(e)} = \left\{ \Gamma_\beta^{(c)} \mid \text{int}(\Gamma_\beta^{(c)}) \cap \text{int}(\Gamma_\alpha^{(e)}) \neq \emptyset, 1 \leq c \leq Nel \right\} \quad (15)$$

where ‘ Nel ’ denotes the number of elements, and $\text{int}(\cdot)$ denotes the interior. For example, common edge set for the finite element edge $\Gamma_4^{(e8)}$ in Fig. 4 is $C_4^{(e8)} = \{ \Gamma_2^{(e4)}, \Gamma_2^{(e5)}, \Gamma_4^{(e8)} \}$. It is denoted by bold line in Fig. 4. Similarly, common edges for $\Gamma_2^{(e1)}$ are $\Gamma_4^{(e6)}$ and $\Gamma_2^{(e1)}$ itself.

Secondly, mismatching element edge is defined with the aid of the common edge concept. The finite element edge $\Gamma_\alpha^{(e)}$ is defined as mismatching edge, if there is any common edge for $\Gamma_\alpha^{(e)}$ which is not identical to $\Gamma_\alpha^{(e)}$ itself. If the sets of nodal points defined in each edge are different, the edges are considered not to be identical even though the line segments of each edge are the same. And the mismatching element boundary $\Gamma_{mis}^{(e)}$ for each element (e) is defined as the union of mismatching element edges for the element (e). For example, the mismatching element boundaries for element ($e3$) and ($e7$) in Fig. 5 are $\Gamma_2^{(e3)} \cup \Gamma_3^{(e3)}$ and $\Gamma_1^{(e7)} \cup \Gamma_4^{(e7)}$, respectively.

If a node of element (e_i) is contained in the mismatching element boundary $\Gamma_{mis}^{(e_i)}$, then the node is called the mismatching node of element (e_i) as shown in Ω_{e5} of Fig. 6. Additionally, if a nodal point of element (e_i) is contained

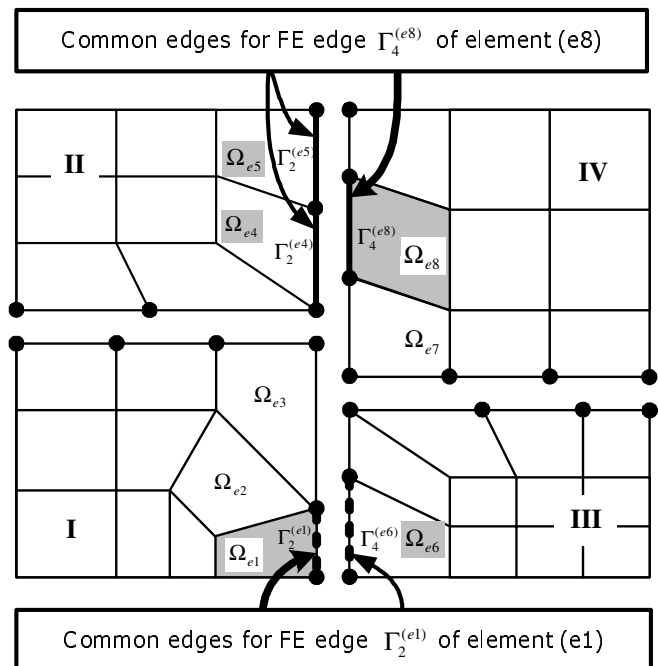


Figure 4 : Explanation of terminology I (common edges for each finite element edge)

in some element (e_j) but it is not the node of the element (e_j) as shown in Ω_{e2} of Fig. 6, then it is also defined as the mismatching node of element (e_i). The index set for the mismatching nodal points for each element (e_i) is denoted by $N_{mis}^{(e_i)}$.

By collecting the mismatching element boundaries over the whole elements, the mismatching interface Γ_{mis} for the given problem can be constructed as shown in Fig. 6.

$$\Gamma_{mis} = \bigcup_{e=1}^{Nel} \Gamma_{mis}^{(e)} \quad (16)$$

where ‘ e ’ and ‘ Nel ’ denote the element number and the number of elements, respectively.

Finally, the index set N_{mis} of mismatching nodal points is defined as the nodal point numbers on the mismatching interfaces. It can be also constructed by collecting the set of mismatching nodal points for each element.

$$\begin{aligned} N_{mis} &= \{k \mid \text{node } \mathbf{x}_k \in \Gamma_{mis}, 1 \leq k \leq Nnode\} \\ &= \bigcup_{e=1}^{Nel} N_{mis}^{(e)} \end{aligned} \quad (17)$$

where ‘ $Nnode$ ’ denotes the total number of nodal points. In Fig. 6, the mismatching nodal points are denoted by hollow circle. The transient element is defined as an element of which boundary has a nonempty intersection with the mismatching interface, and the union of those domains will be called the transient region Ω_{tran} as shown in Fig. 7. Additionally, the union of domains of non-transient elements will be called the compatible region Ω_{comp} , and the intersection between Ω_{tran} and Ω_{comp} will be called the compatible-transient interface. The transient nodal points imply the nodal points located in transient region. Its index set N_{tran} can be written as follows.

$$N_{tran} = \{k \mid \text{node } \mathbf{x}_k \in \Omega_{tran}, 1 \leq k \leq Nnode\} \quad (18)$$

Conversely, the non-transient nodal points means the nodal points outside the transient region, and its index set N_{nont} is as follow.

$$N_{nont} = \{k \mid \text{node } \mathbf{x}_k \notin \Omega_{tran}, 1 \leq k \leq Nnode\} \quad (19)$$

It is noted that the set of non-transient nodal points is not identical to the set of nodal points located in the compatible region Ω_{comp} . Additionally, the transient nodal point

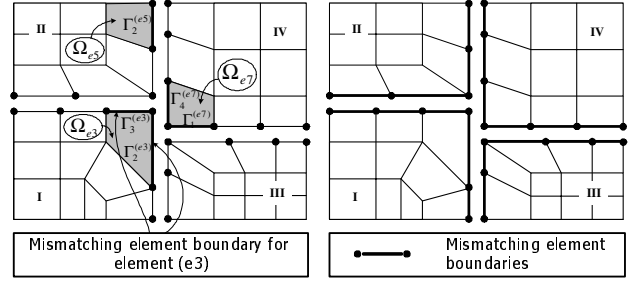


Figure 5 : Terminology II (incompatible element boundary)

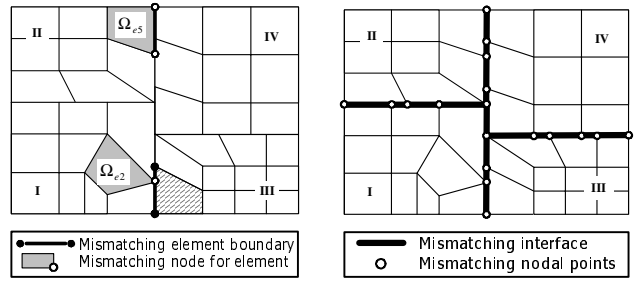


Figure 6 : Terminology III (mismatching interface, mismatching nodal points)

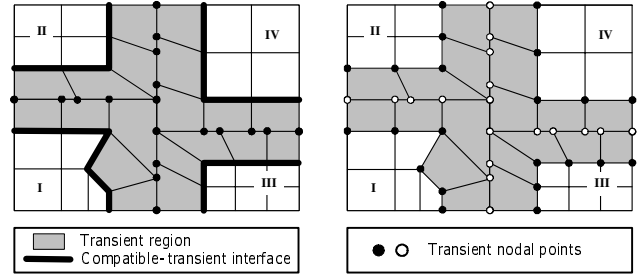


Figure 7 : Terminology IV (Transient region, compatible-transient interface, transient nodal points)

index set and non-transient nodal point index set satisfy the relations as shown below.

$$\begin{cases} N_{tran} \cap N_{nont} = \phi \\ N_{tran} \cup N_{nont} = \{k \mid 1 \leq k \leq Nnode\} \end{cases} \quad (20)$$

3.2 Displacement Welding

In the present displacement welding procedure for coupled analysis of independently modeled substructures, a newly defined nodal shape function is utilized instead of the conventional finite element shape functions for the transient nodal points to eliminate the discontinuity in mismatching interface as written in Eq. (21).

$$\begin{aligned} &\text{For } i \in N_{tran}, \\ &N_i^B(\mathbf{x}) = \begin{cases} \Theta_i^B(\mathbf{x}), \mathbf{x} \in \Omega_{tran} \\ N_i(\mathbf{x}), \mathbf{x} \in \Omega_{comp} \end{cases} \\ &\text{For } i \in N_{nont} \text{ (i.e., } i \notin N_{tran}), \\ &N_i^B(\mathbf{x}) = \begin{cases} N_i(\mathbf{x}) = 0, \mathbf{x} \in \Omega_{tran} \\ N_i(\mathbf{x}), \mathbf{x} \in \Omega_{comp} \end{cases} \end{aligned} \quad (21)$$

where $N_i(\mathbf{x})$ is the finite element shape function, and $\Theta_i^B(\mathbf{x})$ is a blended function defined over the transient region. If the $\Theta_i^B(\mathbf{x})$ is continuous over the transient region Ω_{tran} , then the continuity of nodal shape function across the mismatching interface is guaranteed. Also if $\Theta_i^B(\mathbf{x}) = N_i(\mathbf{x})$ for $\mathbf{x} \in \Omega_{tran} \cap \Omega_{comp}$, then the continuity between the transient and compatible regions can be ensured.

To ensure the continuity across the mismatching and compatible-transient interfaces, the blended function of Eq. (22) is introduced. It is noted that a similar blended form was adopted to couple the meshless system and finite element system in the previous works [Belytschko, Krongauz, and Organ (1996); Chen and Raju (2002)].

$$\begin{aligned} &\text{For } i \in N_{tran}, \\ &\Theta_i^B(\mathbf{x}) = (1 - \lambda(\mathbf{x}))N_i(\mathbf{x}) + \lambda(\mathbf{x})\psi_i(\mathbf{x}) \end{aligned} \quad (22)$$

where $\psi_i(\mathbf{x})$ is the moving least squares nodal shape function obtained from the transient nodal points $\{\mathbf{x}_k | k \in N_{tran}, 1 \leq k \leq Nnode\}$ and it is continuous over the transient region regardless of the mismatching interface. Moreover, it is noted that the moving least squares nodal shape function satisfies the consistency conditions over the transient region as shown in Eq. (23) since the functions are constructed by using the nodal points in transient region.

$$\begin{aligned} &\text{For } \mathbf{x} \in \Omega_{tran}, \\ &\sum_{i \in N_{tran}} \psi_i(\mathbf{x}) = 1 \text{ and } \sum_{i \in N_{tran}} \psi_i(\mathbf{x})\mathbf{x}_i = \mathbf{x} \end{aligned} \quad (23)$$

And the finite element shape functions satisfy the follow-

ing consistency over the whole domain.

$$\begin{aligned} &\text{For } \mathbf{x} \in \Omega = \Omega_{tran} \cup \Omega_{comp}, \\ &\sum_{i=1}^{Nnode} N_i(\mathbf{x}) = 1 \text{ and } \sum_{i=1}^{Nnode} N_i(\mathbf{x})\mathbf{x}_i = \mathbf{x} \end{aligned} \quad (24)$$

Since the finite element shape functions for non-transient nodal points are identically zero over the transient region (i.e., $N_i(\mathbf{x}) = 0$, for $\mathbf{x} \in \Omega_{tran}$ & $i \notin N_{tran}$), Eq. (24) can be reduced to Eq. (25).

$$\begin{aligned} &\text{For } \mathbf{x} \in \Omega_{tran}, \\ &\begin{cases} \sum_{i=1}^{Nnode} N_i(\mathbf{x}) = \sum_{i \in N_{tran}} N_i(\mathbf{x}) = 1 \\ \sum_{i=1}^{Nnode} N_i(\mathbf{x})\mathbf{x}_i = \sum_{i \in N_{tran}} N_i(\mathbf{x})\mathbf{x}_i = \mathbf{x} \end{cases} \end{aligned} \quad (25)$$

The $\lambda(\mathbf{x})$ used in the blended function $\Theta_i^B(\mathbf{x})$ is a continuous function, and it is selected to be '1' on the mismatching interface Γ_{mis} in order to eliminate the discontinuity of finite element shape function on the mismatching interface. Through the selection of $\lambda(\mathbf{x})$, $(1 - \lambda(\mathbf{x}))N_i(\mathbf{x})$ becomes a continuous function of which value is zero on the mismatching interface, and the blended function $\Theta_i^B(\mathbf{x})$ becomes continuous because $\lambda(\mathbf{x})\psi_i(\mathbf{x})$ is also continuous. Also, $\lambda(\mathbf{x})$ is chosen to be '0' on the compatible-transient interface $\Omega_{comp} \cap \Omega_{tran}$ so as to satisfy the displacement compatibility between the transient region Ω_{tran} and the compatible region Ω_{comp} . As a result, the blended nodal shape function satisfies the relation (26).

$$\begin{aligned} &\text{For } i \in N_{tran}, \\ &(i) \Theta_i^B(\mathbf{x}) \text{ is continuous for } \mathbf{x} \in \Omega_{tran} \\ &(ii) \Theta_i^B(\mathbf{x}) = N_i(\mathbf{x}), \mathbf{x} \in \Omega_{comp} \cap \Omega_{tran} \end{aligned} \quad (26)$$

By the relation, one can ensure the compatibility between the compatible region and the transient region. Also the continuity across the mismatching interface can be guaranteed. To obtain the value of $\lambda(\mathbf{x})$ in element-by-element manner, the relation (27) is adopted in the present work.

$$\begin{aligned} &\text{For } \mathbf{x} \in \Omega_e, \\ &\lambda(\mathbf{x}) = \begin{cases} \sum_{i \in N_{mis}^{(e)}} N_i(\mathbf{x}) & \text{if } (\mathbf{x} \in) \Omega_e \subset \Omega_{tran} \\ 0 & \text{if } (\mathbf{x} \in) \Omega_e \not\subset \Omega_{tran} \end{cases} \end{aligned} \quad (27)$$

where $N_{mis}^{(e)}$ denotes the index set of mismatching nodal points for element (e). Ω_e implies the domain of element

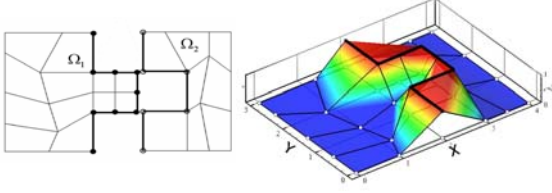


Figure 8 : Typical shape of $\lambda(\mathbf{x})$ for the system of independently modeled substructures

(e). In Fig. 8, typical shape of $\lambda(\mathbf{x})$ obtained from Eq. (27) for the system of independently modeled substructures is presented.

Additionally, one can show that the newly defined nodal shape functions (21) satisfy the consistency conditions as follows. In the derivation of consistency conditions, Eqs. (23)-(25) are utilized along with the fact that the finite element shape functions associated with non-transient nodal points are identically zero over the transient region.

0th order consistency of new shape function

$$\sum_{i=1}^{Nnode} N_i^B(\mathbf{x}) = 1 \quad (28)$$

Proof:

For $\mathbf{x} \in \Omega_{tran}$,

$$\begin{aligned} \sum_{i=1}^{Nnode} N_i^B(\mathbf{x}) &= \sum_{i \in N_{tran}} N_i^B(\mathbf{x}) + \sum_{i \in N_{non}} N_i^B(\mathbf{x}) \\ &\leftarrow N_i^B(\mathbf{x}) = 0 \text{ for } \mathbf{x} \in \Omega_{tran} \text{ and } i \notin N_{tran} \\ &= \sum_{i \in N_{tran}} [(1 - \lambda(\mathbf{x}))N_i(\mathbf{x}) + \lambda(\mathbf{x})\psi_i(\mathbf{x})] \\ &= (1 - \lambda(\mathbf{x})) \sum_{i \in N_{tran}} N_i(\mathbf{x}) + \lambda(\mathbf{x}) \sum_{i \in N_{tran}} \psi_i(\mathbf{x}) \end{aligned}$$

$$\text{Since } \sum_{i \in N_{tran}} N_i(\mathbf{x}) = 1, \sum_{i \in N_{tran}} \psi_i(\mathbf{x}) = 1 \text{ for } \mathbf{x} \in \Omega_{tran}$$

$$\sum_{i=1}^{Nnode} N_i^B(\mathbf{x}) = (1 - \lambda(\mathbf{x})) + \lambda(\mathbf{x}) = 1$$

For $\mathbf{x} \in \Omega_{comp}$,

$$\text{Since } N_i^B(\mathbf{x}) = N_i(\mathbf{x}) \text{ and } \sum_{i=1}^{Nnode} N_i(\mathbf{x}) = 1,$$

$$\sum_{i=1}^{Nnode} N_i^B(\mathbf{x}) = \sum_{i=1}^{Nnode} N_i(\mathbf{x}) = 1$$

Therefore, $\sum_{i=1}^{Nnode} N_i^B(\mathbf{x}) = 1$ for all $\mathbf{x} \in \Omega$.

1st order consistency of new shape function

$$\sum_{i=1}^{Nnode} N_i^B(\mathbf{x})\mathbf{x}_i = \mathbf{x} \quad (29)$$

Proof:

For $\mathbf{x} \in \Omega_{tran}$,

$$\begin{aligned} \sum_{i=1}^{Nnode} N_i^B(\mathbf{x})\mathbf{x}_i &= \sum_{i \in N_{tran}} N_i^B(\mathbf{x})\mathbf{x}_i + \sum_{i \in N_{non}} N_i^B(\mathbf{x})\mathbf{x}_i \\ &\leftarrow N_i^B(\mathbf{x}) = 0 \text{ for } \mathbf{x} \in \Omega_{tran} \text{ and } i \notin N_{tran} \\ &= \sum_{i \in N_{tran}} [(1 - \lambda(\mathbf{x}))N_i(\mathbf{x})\mathbf{x}_i + \lambda(\mathbf{x})\psi_i(\mathbf{x})\mathbf{x}_i] \\ &= (1 - \lambda(\mathbf{x})) \sum_{i \in N_{tran}} N_i(\mathbf{x})\mathbf{x}_i + \lambda(\mathbf{x}) \sum_{i \in N_{tran}} \psi_i(\mathbf{x})\mathbf{x}_i \end{aligned}$$

$$\text{Since } \sum_{i \in N_{tran}} N_i(\mathbf{x})\mathbf{x}_i = \mathbf{x}, \sum_{i \in N_{tran}} \psi_i(\mathbf{x})\mathbf{x}_i = \mathbf{x} \text{ for } \mathbf{x} \in \Omega_{tran}$$

$$\sum_{i=1}^{Nnode} N_i^B(\mathbf{x})\mathbf{x}_i = (1 - \lambda(\mathbf{x}))\mathbf{x} + \lambda(\mathbf{x})\mathbf{x} = \mathbf{x}$$

For $\mathbf{x} \in \Omega_{comp}$,

$$\text{Since } N_i^B(\mathbf{x}) = N_i(\mathbf{x}) \text{ and } \sum_{i=1}^{Nnode} N_i(\mathbf{x})\mathbf{x}_i = \mathbf{x},$$

$$\sum_{i=1}^{Nnode} N_i^B(\mathbf{x})\mathbf{x}_i = \sum_{i=1}^{Nnode} N_i(\mathbf{x})\mathbf{x}_i = \mathbf{x}$$

Therefore, $\sum_{i=1}^{Nnode} N_i^B(\mathbf{x})\mathbf{x}_i = \mathbf{x}$ for all $\mathbf{x} \in \Omega$.

It is noted that the necessary conditions for describing the rigid body and constant strain modes are ensured through the consistency conditions.

3.3 Weak Form and Its Approximation

Let us consider the general linear elastic problem in domain Ω . Then the weak form of equilibrium equation can be written in engineering matrix notation as follows.

$$\int_{\Omega} \delta \boldsymbol{\varepsilon}^T \mathbf{D} \boldsymbol{\varepsilon} d\Omega = \int_{\Omega} \delta \mathbf{u}^T \mathbf{f} d\Omega + \int_{\partial\Omega_t} \delta \mathbf{u}^T \bar{\mathbf{t}} d\Gamma \quad (30)$$

where \mathbf{u} , $\boldsymbol{\varepsilon}$, \mathbf{f} and $\bar{\mathbf{t}}$ denote displacement, strain, force per unit volume and traction, respectively. \mathbf{D} is the elastic modulus matrix, and $\partial\Omega_t$ is the traction boundary. Assume that the elastic body is modeled by several substructures with mismatching interfaces as shown in Fig. 4. Then the weak form may be rewritten as the form of Eq. (31), since the integral domain of weak form can

be divided into the transient region and the compatible region of substructures. For $\mathbf{x} \in \Omega_{comp}$,

$$\begin{aligned} & \int_{\Omega_{comp}} \delta \boldsymbol{\varepsilon}^T \mathbf{D} \boldsymbol{\varepsilon} d\Omega + \int_{\Omega_{tran}} \delta \boldsymbol{\varepsilon}^T \mathbf{D} \boldsymbol{\varepsilon} d\Omega \\ &= \int_{\Omega_{comp}} \delta \mathbf{u}^T \mathbf{f} d\Omega + \int_{\Omega_{tran}} \delta \mathbf{u}^T \mathbf{f} d\Omega \\ &+ \int_{\partial\Omega_i \cap \Omega_{comp}} \delta \mathbf{u}^T \bar{\mathbf{t}} d\Gamma + \int_{\partial\Omega_i \cap \Omega_{tran}} \delta \mathbf{u}^T \bar{\mathbf{t}} d\Gamma \end{aligned} \quad (31)$$

$$\begin{aligned} \begin{Bmatrix} u \\ v \end{Bmatrix} &\cong \sum_{i \in N_{nont}} \begin{bmatrix} N_i & 0 \\ 0 & N_i \end{bmatrix} \begin{Bmatrix} u_i \\ v_i \end{Bmatrix} \\ &+ \sum_{i \in N_{tran}} \begin{bmatrix} N_i & 0 \\ 0 & N_i \end{bmatrix} \begin{Bmatrix} u_i \\ v_i \end{Bmatrix} \\ &= [\mathbf{N}_{nont} \quad \mathbf{N}_{tran}] \begin{Bmatrix} \mathbf{U}_{nont} \\ \mathbf{U}_{tran} \end{Bmatrix} = \mathbf{N} \mathbf{U} \end{aligned} \quad (34)$$

In case of two dimension, the displacement and strain fields in Eq. (31) are approximated by the newly introduced blended nodal shape function $N_i^B(\mathbf{x})$ as denoted in Eq. (32) and (33).

$$\begin{aligned} \begin{Bmatrix} u(\mathbf{x}) \\ v(\mathbf{x}) \end{Bmatrix} &\cong \sum_{i=1}^{Nnode} \begin{bmatrix} N_i^B(\mathbf{x}) & 0 \\ 0 & N_i^B(\mathbf{x}) \end{bmatrix} \begin{Bmatrix} u_i \\ v_i \end{Bmatrix} \\ &= \sum_{i \in N_{nont}} \begin{bmatrix} N_i^B & 0 \\ 0 & N_i^B \end{bmatrix} \begin{Bmatrix} u_i \\ v_i \end{Bmatrix} \\ &+ \sum_{i \in N_{tran}} \begin{bmatrix} N_i^B & 0 \\ 0 & N_i^B \end{bmatrix} \begin{Bmatrix} u_i \\ v_i \end{Bmatrix} \\ &= [\mathbf{N}_{nont}^B \quad \mathbf{N}_{tran}^B] \begin{Bmatrix} \mathbf{U}_{nont} \\ \mathbf{U}_{tran} \end{Bmatrix} \\ &= \mathbf{N}_B \mathbf{U} \end{aligned} \quad (32)$$

For $\mathbf{x} \in \Omega_{comp}$,

$$\begin{aligned} \begin{Bmatrix} \varepsilon_{xx} \\ \varepsilon_{yy} \\ \gamma_{xy} \end{Bmatrix} &\cong \sum_{i \in N_{nont}} \begin{bmatrix} \frac{\partial N_i}{\partial x} & 0 \\ 0 & \frac{\partial N_i}{\partial y} \\ \frac{\partial N_i}{\partial y} & \frac{\partial N_i}{\partial x} \end{bmatrix} \begin{Bmatrix} u_i \\ v_i \end{Bmatrix} \\ &+ \sum_{i \in N_{tran}} \begin{bmatrix} \frac{\partial N_i}{\partial x} & 0 \\ 0 & \frac{\partial N_i}{\partial y} \\ \frac{\partial N_i}{\partial y} & \frac{\partial N_i}{\partial x} \end{bmatrix} \begin{Bmatrix} u_i \\ v_i \end{Bmatrix} \\ &= [\mathbf{B}_{nont} \quad \mathbf{B}_{tran}] \begin{Bmatrix} \mathbf{U}_{nont} \\ \mathbf{U}_{tran} \end{Bmatrix} = \mathbf{B} \mathbf{U} \end{aligned} \quad (35)$$

Similarly, the approximations in the transient region can be rewritten as follows because only the shape functions associated with transient nodal points are not zero in the transient region.

For $\mathbf{x} \in \Omega_{tran}$,

$$\begin{aligned} \begin{Bmatrix} u \\ v \end{Bmatrix} &\cong \sum_{i \in N_{tran}} \begin{bmatrix} \Theta_i^B & 0 \\ 0 & \Theta_i^B \end{bmatrix} \begin{Bmatrix} u_i \\ v_i \end{Bmatrix} \\ &= [\mathbf{0} \quad \Theta_{tran}^B] \begin{Bmatrix} \mathbf{U}_{comp} \\ \mathbf{U}_{tran} \end{Bmatrix} = \Theta_B \mathbf{U} \end{aligned} \quad (36)$$

For $\mathbf{x} \in \Omega_{tran}$

$$\begin{aligned} \begin{Bmatrix} \varepsilon_{xx} \\ \varepsilon_{yy} \\ \gamma_{xy} \end{Bmatrix} &\cong \sum_{i \in N_{tran}} \begin{bmatrix} \frac{\partial \Theta_i^B}{\partial x} & 0 \\ 0 & \frac{\partial \Theta_i^B}{\partial y} \\ \frac{\partial \Theta_i^B}{\partial y} & \frac{\partial \Theta_i^B}{\partial x} \end{bmatrix} \begin{Bmatrix} u_i \\ v_i \end{Bmatrix} \\ &= [\mathbf{0} \quad \Xi_{tran}^B] \begin{Bmatrix} \mathbf{U}_{comp} \\ \mathbf{U}_{tran} \end{Bmatrix} = \Xi_B \mathbf{U} \end{aligned} \quad (37)$$

Considering the fact that the blended shape function $N_i^B(\mathbf{x})$ is the same as the original finite element shape function $N_i(\mathbf{x})$ in the compatible region, the approximated forms for the displacement and strain fields in the compatible region are rewritten as Eq. (34) and Eq. (35), respectively.

Substitution of Eqs. (34-37) into Eq. (31) gives a relation as shown below.

For all $\delta \mathbf{U}$,

$$\begin{aligned}
 & \delta \mathbf{U}^T \left(\int_{\Omega_{comp}} \mathbf{B}^T \mathbf{D} \mathbf{B} d\Omega \right) \mathbf{U} + \delta \mathbf{U}^T \left(\int_{\Omega_{tran}} \Xi_B^T \mathbf{D} \Xi_B d\Omega \right) \mathbf{U} \\
 &= \delta \mathbf{U}^T \left\{ \int_{\Omega_{comp}} \mathbf{N}^T \mathbf{f} d\Omega \right\} \\
 &+ \delta \mathbf{U}^T \left\{ \int_{\partial\Omega_t \cap \Omega_{comp}} \mathbf{N}^T \bar{\mathbf{t}} d\Gamma \right\} \\
 &+ \delta \mathbf{U}^T \left\{ \int_{\Omega_{tran}} \Theta_B^T \mathbf{f} d\Omega \right\} \\
 &+ \delta \mathbf{U}^T \left\{ \int_{\partial\Omega_t \cap \Omega_{tran}} \Theta_B^T \bar{\mathbf{t}} d\Gamma \right\} \quad (38)
 \end{aligned}$$

Since the Eq. (38) should hold for all $\delta \mathbf{U}$, one can obtain the following system of linear algebraic equations.

$$(\mathbf{K}_{comp} + \mathbf{K}_{tran}) \mathbf{U} = \mathbf{F}_{comp} + \mathbf{F}_{tran} \quad (39)$$

where the subscripts ‘*comp*’ and ‘*tran*’ imply the terms originated from the compatible and transient regions, respectively. In implementation, a higher order Gauss numerical integration is utilized for the transient region, since the moving least squares function is rational function [Atluri, Cho, and Kim (1999); Dolbow and Belytschko (1999)]. Also other numerical integration schemes may be considered for the transient region [Chen, Wu, Yoon, and You (2001); Atluri, Han, and Rajendran (2004); Han and Atluri (2004)].

It should be noted that the terms \mathbf{K}_{comp} and \mathbf{F}_{comp} from the compatible region are exactly the same as the original finite element system. And the terms, that should be modified for coupled analysis, are related to only the limited number of transient nodal points in transient domain as shown below.

$$\begin{aligned}
 \mathbf{K}_{tran} \mathbf{U} &= \begin{bmatrix} \mathbf{0} & \mathbf{0} \\ \mathbf{0} & \int_{\Omega_{tran}} (\Xi_B^B)^T \mathbf{D} \Xi_B^B d\Omega \end{bmatrix} \begin{Bmatrix} \mathbf{U}_{nont} \\ \mathbf{U}_{tran} \end{Bmatrix} \\
 \mathbf{F}_{tran} &= \begin{Bmatrix} \mathbf{0} \\ \left(\int_{\Omega_{tran}} (\Theta_B^B)^T \mathbf{f} d\Omega + \int_{\partial\Omega_t \cap \Omega_{tran}} (\Theta_B^B)^T \bar{\mathbf{t}} d\Gamma \right) \end{Bmatrix} \quad (40)
 \end{aligned}$$

Therefore, one can carry out the coupled analysis of the integrated whole model of independently modeled substructures by simple replacement of the stiffness matrix and the load vector for transient region as shown in Fig. 9. Also, unlike the Lagrange multiplier approaches, the

proposed displacement welding procedure does not require any additional unknown, and preserves the positive definiteness and banded structure of the system stiffness matrix, since the incompatible displacement fields in the transient region for mismatching interface of independently modeled substructures are directly welded into a compatible displacement field over the whole model.

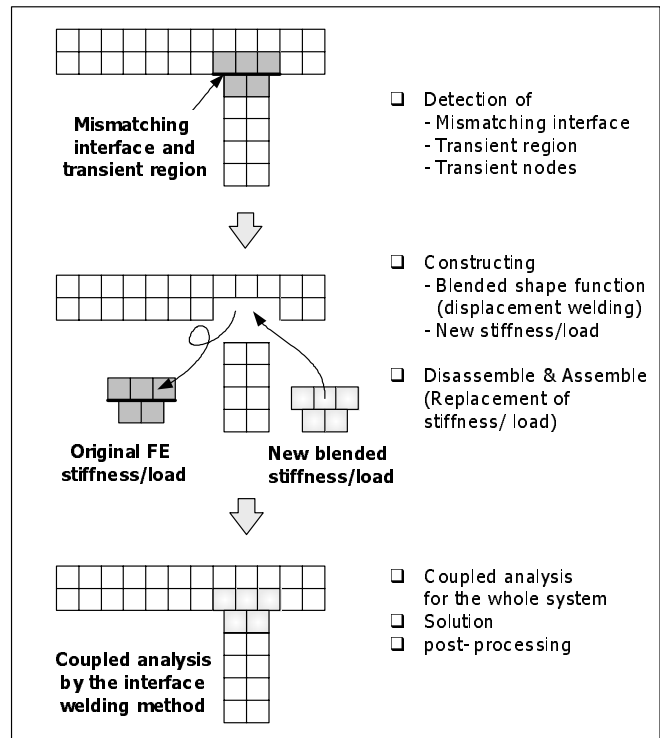


Figure 9 : Coupled analysis by displacement welding

4 Numerical Examples

4.1 Patch Test

In this section, patch tests are carried out to prove the validity of the currently proposed welding technique. In patch tests, two models in Fig. 10 and Fig. 11 are considered. The first model in Fig. 10 consists of three substructures and has two mismatching interfaces. And the second model in Fig. 11 consists of three substructures and has three mismatching interfaces.

Young’s modulus and Possion’s ratio are $E=10$ and $\nu = 0.3$, respectively. Because the newly constructed blended nodal shape function in the transient region is a rational function, the function may not be integrated accurately. Therefore, we investigate the effect of Gaussian integra-

Table 1 : Results of patch test for model I according to Gaussian quadrature order. (Displacement of node A)

	u	v
Gauss order	1.2 (exact))	-0.24 (exact)
2×2	1.2137729261	-0.25994973813
4×4	1.2004204015	-0.24037344008
8×8	1.2000420922	-0.24006613642
16×16	1.1999945714	-0.23999102101
32×32	1.2000004006	-0.24000052754

Table 2 : Results of patch test for model II according to Gaussian quadrature order. (Displacement of node B)

	u	v
Gauss order	0.6 (exact)	-0.18 (exact)
2×2	0.61289027104	-0.1816811702
4×4	0.60000209594	-0.1800195193
8×8	0.59999398587	-0.1799923851
16×16	0.59999512494	-0.1799946816
32×32	0.59999515627	-0.1799946985

tion order on the results of the patch tests. As presented in table 1 and table 2, one can identify that the numerical solution is getting improved as the integration order is increased. Also it is observed that more than 8×8 points integration scheme gives quite acceptable solution in practical sense. Based on the the observation, 8×8 points integration rule is adopted for other numerical examples.

In Fig. 12, the deformed shapes for patch tests are presented. The results show that the proposed method passes the patch tests successfully in practical sense.

4.2 Beam Type Problem

To investigate the convergence of the proposed welding technique, a cantilevered beam type problem is analyzed. The model is presented in Fig. 13.

The traction force $P = 1000$ is applied to the righthand side of the beam, and displacement boundary condition is enforced on the lefthand side of the beam. The exact solutions are given as follows.

$$u = \frac{P}{6EI} \left(y - \frac{h}{2} \right) [3x(x - 2l) + (v + 2)(h - y)y] \quad (41)$$

$$v = \frac{P}{6EI} \left[x^2(3l - x) - 3v(x - l)\left(y - \frac{h}{2}\right)^2 + (4 + 5v)\frac{h^2}{4}x \right]$$

Table 3 : Error norms for each mesh division

Case	Mesh Size $\Omega_1 \times \Omega_2$	L_2 Norm	H^1 Norm
1	0.25×0.5	3.40428×10^{-2}	1.59251×10^{-1}
2	0.125 × 0.25	8.98999×10^{-3}	8.19196×10^{-2}
3	0.0625×0.125	2.29263×10^{-3}	4.13342×10^{-2}
4	0.03125×0.0625	5.73131×10^{-4}	2.08571×10^{-2}

(42)

$$\sigma_{xx} = \frac{P}{I}(x - L)\left(y - \frac{h}{2}\right) \quad (43)$$

$$\sigma_{yy} = 0 \quad (44)$$

$$\sigma_{xy} = \frac{Py}{2I}\left(\frac{h}{2} - y\right) \quad (45)$$

Young’s modulus and Poisson’s ratio are $E = 1 \times 10^7$ and $\nu = 0.3$, respectively. The mismatching interface is located at $x = 5.0$, and initial mesh sizes for each substructure are $h_1 = 0.25$ and $h_2 = 0.5$, respectively. The 4 node bilinear elements are used. For convergence test, meshes in each sub-domain are refined, and the results are presented in Fig. 14 and table 3. The convergence rates for the L_2 norm and H^1 norm [Atluri, Cho, and Kim (1999)] are 2 and 1, respectively.

In Fig. 15, typical deformed shape obtained by the coupled analysis of whole model is presented. The figure clearly shows that the whole model with mismatching interface is deformed just like the compatible model if the proposed welding technique is utilized for coupled analysis.

4.3 Infinite Plate with Circular Hole

In this section, the infinite plate with a circular hole is analyzed through the proposed welding technique. As presented in Fig. 16, the center part around the hole is independently modeled. The displacement boundary condition is enforced on both of the lefthand side and bottom side of the model because of its symmetry, and the exact traction obtained from the exact solution is applied to the righthand side and upper side of the finite model. Young’s modulus and Poisson’s ratio are $E = 3 \times 10^7$ and $\nu = 0.3$, respectively.

The exact solutions for this problem are given as follows.

$$u = \frac{1 + \nu}{E} \left(\frac{1}{1 + \nu} r \cos \theta + \frac{2}{1 + \nu} \frac{a^2}{r} \cos \theta + \frac{1}{2} \frac{a^2}{r} \cos 3\theta - \frac{1}{2} \frac{a^4}{r^3} \cos 3\theta \right) \quad (46)$$

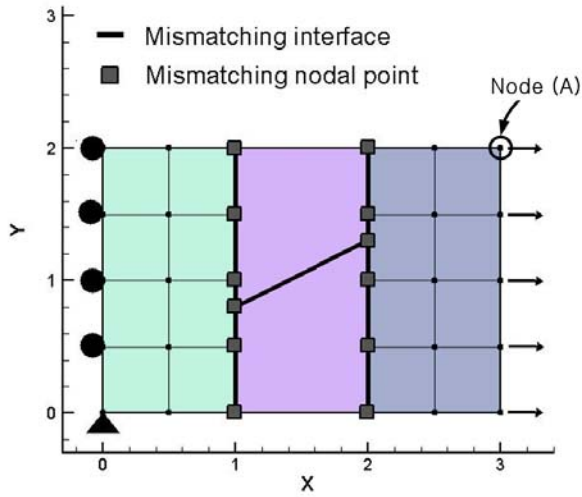


Figure 10 : The patch test model I

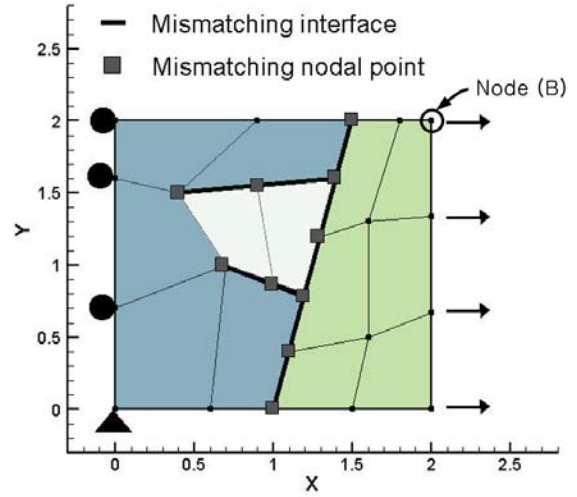


Figure 11 : The patch test model II

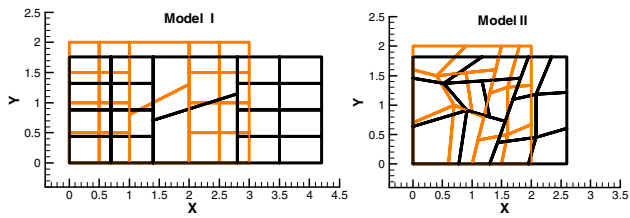


Figure 12 : Deformed shapes obtained from patch tests

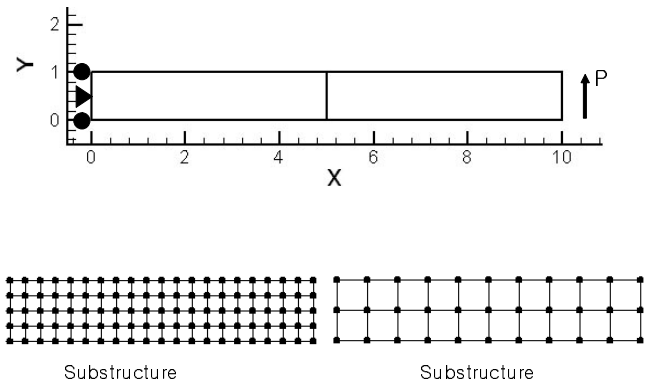


Figure 13 : Beam type model with mismatching interface

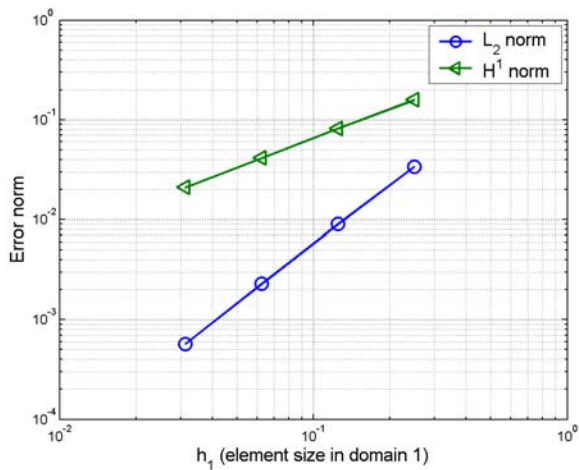


Figure 14 : Convergence rates for L_2 and H^1 error norms

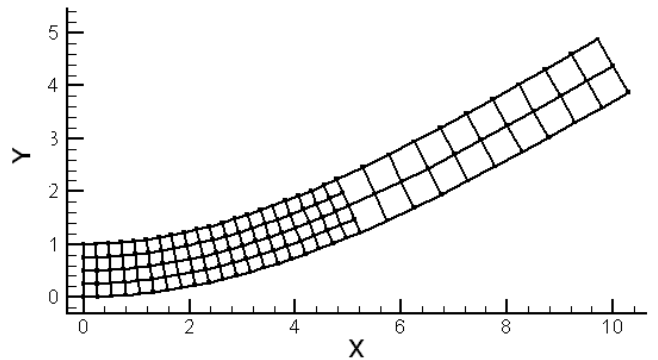


Figure 15 : Deformed shape obtained by the coupled analysis of whole model

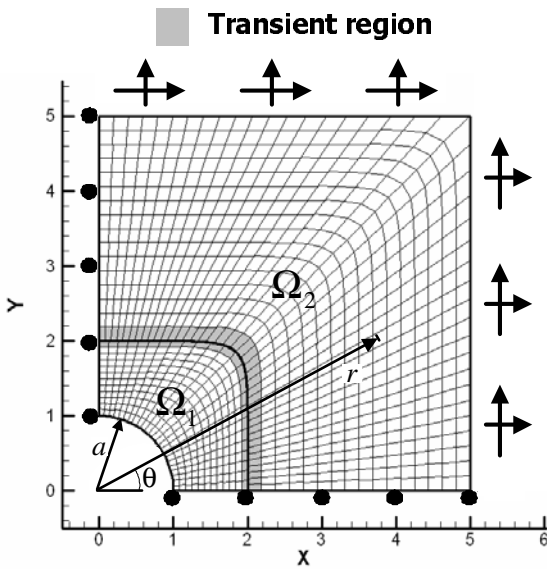


Figure 16 : Plate with a circular hole made of two sub-structures.

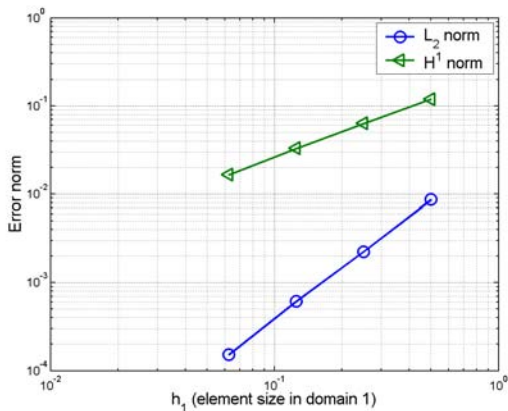


Figure 17 : Convergence rates for L₂ and H₁ error norms.

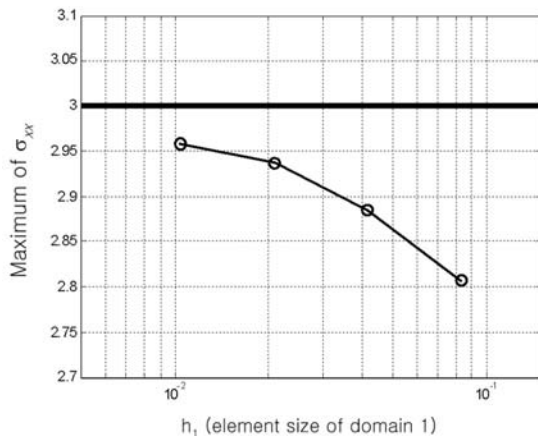


Figure 18 : Maximum value of σ_{xx} near the hole

Table 4 : Error norms for each mesh division

	Mesh Division		L ₂ Norm	H ¹ Norm
	Ω_1	Ω_2		
1	3X6	4X10	8.6871×10^{-3}	1.1947×10^{-1}
2	6X12	8X20	2.2504×10^{-3}	6.3333×10^{-2}
3	12X24	16X40	6.1445×10^{-4}	3.2855×10^{-2}
4	24X48	32X80	1.5187×10^{-4}	1.6505×10^{-2}

$$v = \frac{1 + \nu}{E} \left(\frac{-\nu}{1+\nu} r \sin \theta - \frac{1-\nu}{1+\nu} \frac{a^2}{r} \sin \theta + \frac{1}{2} \frac{a^2}{r} \sin 3\theta - \frac{1}{2} \frac{a^4}{r^3} \sin 3\theta \right) \quad (47)$$

$$\sigma_{xx} = \left(1 - \frac{a^2}{r^2} \left(\frac{3}{2} \cos 2\theta + \cos 4\theta \right) + \frac{3}{2} \frac{a^4}{r^4} \cos 4\theta \right) \quad (48)$$

$$\sigma_{yy} = \left(-\frac{a^2}{r^2} \left(\frac{1}{2} \cos 2\theta - \cos 4\theta \right) - \frac{3}{2} \frac{a^4}{r^4} \cos 4\theta \right) \quad (49)$$

$$\sigma_{xy} = \left(-\frac{a^2}{r^2} \left(\frac{1}{2} \sin 2\theta + \sin 4\theta \right) + \frac{3}{2} \frac{a^4}{r^4} \sin 4\theta \right) \quad (50)$$

The error norms are presented in table 4, and the convergence rates are plotted in Fig. 17. In table 4, mesh division ($n_r \times n_\theta$) means that the domain is divided by n_r -elements in the radial direction and n_θ -elements in the circumferential direction, respectively. Similar to the case of beam type problem, the convergence rates for the L₂ norm and the H¹ norm are 2 and 1, respectively.

Fig. 18 shows the improvement of maximum stress value of σ_{xx} near the hole according to the mesh refinement. As the mesh is refined more and more, the maximum stress value approaches the exact stress value ($\sigma_{max} = 3$). From the numerical results, one can confirm the validity and convergence of the proposed displacement welding technique.

4.4 FE Model with Multiple Substructures

In this section, coupled analysis of finite element model with multiple substructures is carried out. L-shaped beam type problems with various substructures are analyzed by the proposed displacement welding technique, and the numerical solutions are compared with that of conventional finite element method.

In Fig. 19-21, three models are presented. Each model consists of several substructures of which interfaces are not matched with each other. For all of the models,

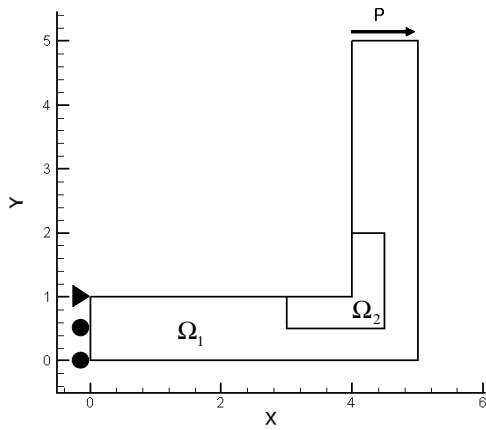


Figure 19 : L-shaped beam model I composed of two substructures.

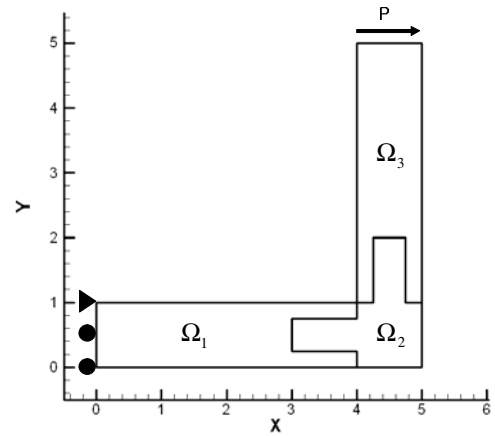


Figure 20 : L-shaped beam model II composed of three substructures.

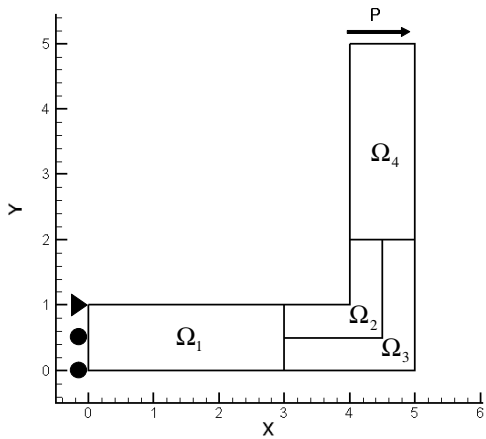


Figure 21 : L-shaped beam model III composed of four substructures.

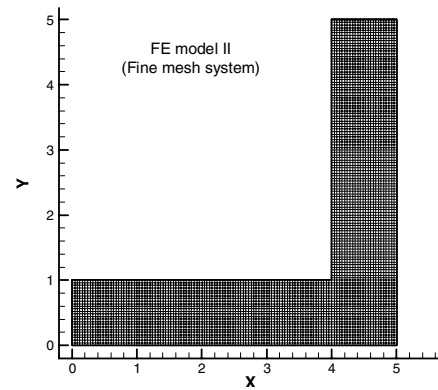


Figure 22 : Finite element model with fine meshes (FE model II)

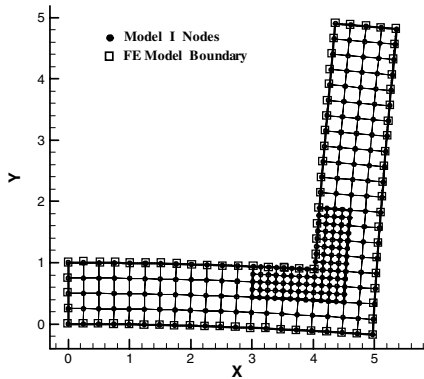


Figure 23 : Comparison of deformed shapes for the Model I and the fine mesh FE model (FEM II).

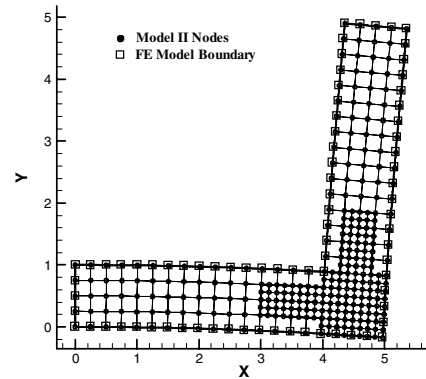


Figure 24 : Comparison of deformed shapes for the Model II and the fine mesh FE model (FEM II).

Table 5 : The size of mesh and total number of elements for each model.

	Ω_1	Ω_2	Ω_3	Ω_4	No. of Elements
Model I	0.25	0.125	-	-	204
Model II	0.25	0.125	0.25	-	240
Model III	0.25	0.0714	0.125	0.25	516

Table 6 : Comparison of numerical solutions : u and v are displacements at upper right tip of the model.

	u	v
FEM I	0.3576	-0.1872
FEM II	0.3659	-0.1897
Model I	0.3636	-0.1886
Model II	0.3621	-0.1883
Model III	0.3648	-0.1886

Young’s modulus E of 3×10^7 and Poisson’s ratio ν of 0.3 are used. The shear force $P=8000$ is applied to the upper side of the model, and displacement boundary condition is enforced on the lefthand side of the model.

In table 5, the size of mesh and the total number of elements for each model are presented. Additionally, conventional finite element analyses are carried out for both of coarse mesh system and fine mesh system, in order to compare the accuracy of numerical solutions. In case of coarse mesh (FEM I), the size of mesh is 0.25, and the total number of element is 144. In case of fine mesh (FEM II) in Fig. 22, the size of mesh is 0.04, and the total number of elements is 5625.

In table 6, the tip displacements obtained by each method are presented, and the deformed shapes of each model are presented in Fig. 23-25. The results show that numerical solutions obtained by the proposed welding method are more accurate compared to the case of coarse mesh (FEM I), and comparable to the numerical solution obtained by the fine mesh system (FEM II).

It means that the current welding technique makes it possible to improve the numerical solution greatly by simply substituting the fine mesh substructure for the region of stress concentration without considering the nodal compatibility between the original finite element model. Additionally, the result, that the first case (model I) is more accurate compared to the second case (model II) even

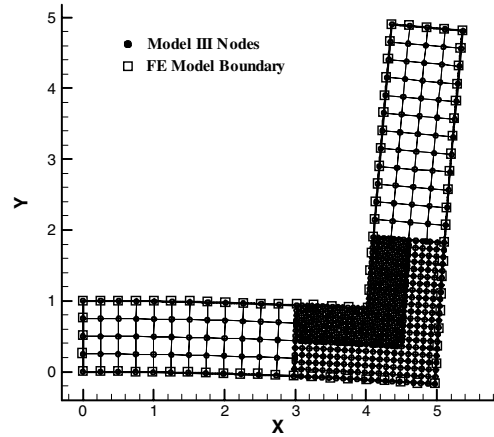


Figure 25 : Comparison of deformed shapes for the Model III and the fine mesh FE model (FEM II)

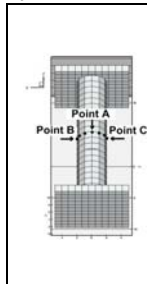
though the total number of element of the first case is smaller than that of the second case, shows that an adequate refinement in the region of stress concentration is essential to obtain enhanced numerical solution.

4.5 Three Dimensional Coupled Analysis

Preliminary example of 3D coupled analysis is worked out to observe the potential and usefulness of the proposed method in practical design and analysis procedures. As shown in Fig. 26, three independently modeled 3D substructures are considered. The nodal points between cylindrical and rectangular sub-structures are not matched with each other, and it is difficult to satisfy the nodal compatibility in the mismatching interface only with the regular shaped elements. Therefore, considerable efforts may be paid if remeshing procedure or conventional transition element method is adopted for

Table 7 : Comparison of deflections at the center of cylindrical substructure.

	Proposed	FE model 1	FE model 2
A	-0.317077	-0.312665	-0.317344
B	-0.322968	-0.318474	-0.322442
C	-0.322970	-0.318475	-0.322443



coupled analysis. However, if the proposed method is used, then the coupled analysis can be carried out with no remeshing, no interface mesh, and no additional unknown. The only process required in the proposed displacement welding technique is a simple replacement of stiffness matrix originated from the transient region regardless of the nodal incompatibility.

In the analysis, fixed boundary condition is applied to the bottoms of two rectangular substructures, and line load is applied to the center of cylindrical substructure. In table 7, the result obtained from the coupled analysis by the proposed method is presented, and compared with the solutions obtained from the compatible finite element models in Fig. 27. In Fig. 28, the deformed configuration obtained by coupled analysis through the proposed displacement welding technique is presented. The result clearly shows a potential and practical usefulness of the proposed method. It is expected that the proposed method can be efficiently utilized in complex 3D coupled analysis if further studies on 3D problems are carried out as a forthcoming research effort.

5 Conclusions

In this work, a novel displacement welding technique is proposed for coupled analysis of independently modeled finite element substructures. In this method, the discontinuity of displacement field at the mismatching interface is eliminated by a new blended function, while preserving the consistency of the displacement field. The blended function is constructed by combining the moving least squares nodal shape function and the original finite element shape function. And the meshless character of the moving least squares nodal shape function makes it possible to weld the incompatible displacement fields easily without any remeshing job or special treatment. Moreover, the proposed welding technique does not introduce any additional unknown, and preserves the favorable positive-definiteness and banded structure of the system stiffness matrix unlike the Lagrange multiplier approaches.

Various numerical tests are carried out, and it is observed that the acceptable results can be obtained by using the proposed welding technique. Additionally, it is known that the proposed method is also highly useful in improving the numerical solution by substituting the fine mesh substructures for the region of stress concentration with no regard to the nodal compatibility between the origi-

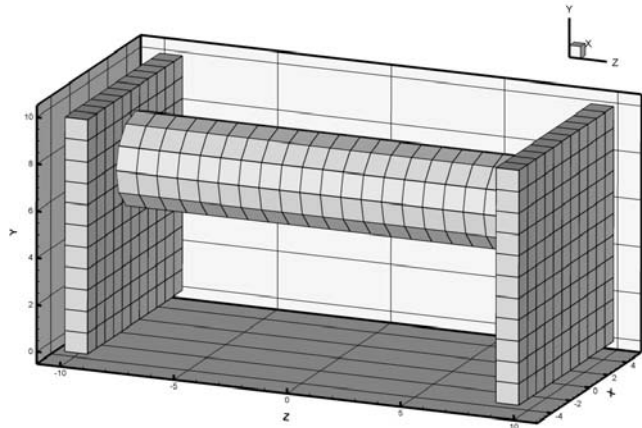


Figure 26 : Structural system composed of three independently modeled substructures with incompatible interfaces. (722 elements, 1332 nodes)

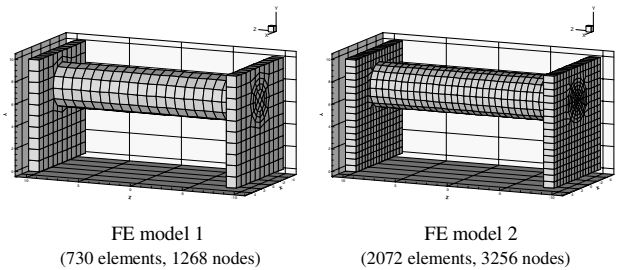


Figure 27 : Compatible finite element models

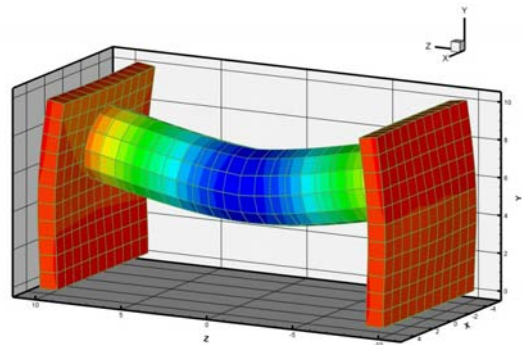


Figure 28 : Deformed shape obtained from 3D coupled analysis of independently modeled substructures with incompatible interfaces (scale factor 5)

nal finite element model. From the results, it is identified that the proposed technique can be efficiently utilized in the coupled analysis of independently modeled finite element substructures.

Acknowledgement: This work was supported by the Korea Research Foundation Grant. (KRF-2003-041-D20101) Authors would like to acknowledge the financial support from the Korea Research Foundation.

References

- Aminpour, M.A.; Pageau, S.; Shin, Y.** (2001): Improved interface modeling technology. *Proceeding of 42nd AIAA/ASME/ASCE/AHS/ASC Structures, Structural Dynamics, and Material Conference*, Paper No. AIAA-2001-1548.
- Aminpour, M.A.; Ransom, J.B.; McCleary, S.L.** (1995): A coupled analysis method for structures with independently modeled finite element subdomains. *International Journal for Numerical Methods in Engineering*, Vol.38, pp. 3695-3718.
- Atluri, S.N.** (2004): *The Meshless Local-Petrov-Galerkin Method for Domain & BIE Discretizations*. Tech Science Press, Forsyth, GA.
- Atluri, S.N.; Cho, J.Y.; Kim, H.G.** (1999): Analysis of thin beams, using the meshless local Petrov-Galerkin method, with generalized moving least squares interpolations. *Computational Mechanics*, Vol. 24, pp. 334-347.
- Atluri, S.N.; Han, Z.D.; Rajendran, A.M.** (2004): A new implementation of the meshless finite volume method through the MLPG "mixed" approach. *CMES: Computer Modeling in Engineering & Sciences*, Vol. 6, pp. 491-513.
- Atluri, S.N.; Shen, S.** (2002): *The Meshless Local-Petrov-Galerkin (MLPG) Method*. Tech Science Press, Forsyth, GA.
- Atluri, S.N.; Zhu, T.** (1998): A new meshless local Petrov-Galerkin (MLPG) approach in computational mechanics. *Computational Mechanics*, Vol. 22, pp. 117-127.
- Babuska, I.; Melenk, J.** (1997): The partition of unity method. *International Journal for Numerical Methods in Engineering*, Vol. 40, pp. 727-758.
- Bathe, K.J.** (1996): *Finite Element Procedures*. International Ed., Prentice-Hall, Englewood Cliffs, NJ.
- Belytschko, T.; Krongauz, Y.; Organ, D.** (1996): Meshless methods: an overview and recent developments. *Computer Method in Applied Mechanics and Engineering*, Vol. 139, pp. 3-47.
- Chen, J.S.; Wu, C.T.; Yoon, S.; You, Y.** (2001): A stabilized conforming nodal integration for Galerkin mesh-free methods. *International Journal for Numerical Methods in Engineering*, Vol. 50, pp. 435-466.
- Chen, T.; Raju, I.S.** (2002): Coupling finite element and meshless local Petrov-Galerkin methods for two-dimensional potential problems. *Proceeding of 43rd AIAA/ASME/ASCE/AHS/ASC Structures, Structural Dynamics, and Material Conference*, Paper No. AIAA-2002-1659
- Dolbow, J.; Belytschko, T.** (1999): Numerical integration of the Galerkin weak form in meshfree methods. *Computational Mechanics*, Vol. 23, pp. 219-230.
- Farhat, C.; Mandel, J.** (1998): The two-level FETI method for static and dynamic plate problems, Part I: An optimal iterative solver for biharmonic systems. *Computer Method in Applied Mechanics and Engineering*, Vol. 155, pp. 129-151.
- Han, Z.D.; Atluri, S.N.** (2004): Meshless local Petrov-Galerkin (MLPG) approaches for solving 3D problems in elasto-statics. *CMES: Computer Modeling in Engineering & Sciences*, Vol. 6, pp. 169-188.
- Han, Z.D.; Atluri, S.N.** (2004): A meshless local Petrov-Galerkin (MLPG) approach for 3-dimensional elasto-dynamics. *CMC: Computers Materials & Continua*, Vol. 1, pp. 129-140.
- Kim, H.G.** (2002): Interface element method (IEM) for a partitioned system with non-matching interfaces. *Computer Method in Applied Mechanics and Engineering*, Vol. 191, pp. 3165-3194.
- Lancaster, P.; Salkauskas, K.** (1981): Surfaces generated by moving least squares methods. *Mathematics of Computation*, Vol. 37, pp. 141-158.
- Li, Q.; Shen, S.; Han, Z.D.; Atluri, S.N.** (2003): Application of meshless local Petrov-Galerkin (MLPG) to problems with singularities, and material discontinuities, in 3D elasticity. *CMES-Computer Modeling in Engineering & Sciences*, Vol. 4, pp. 571-586.
- Liu, W.; Jun, S.; Zhang, Y.** (1995): Reproducing kernel particle methods. *International Journal for Numerical Methods in Fluid*, Vol. 20, pp. 1081-1106.

Nayroles, B.; Touzot, G.; Villon, P. (1992): Generalizing the finite element method: diffuse approximation and diffuse elements. *Computational Mechanics*, Vol. 10, pp. 307-318.

Park, K.C.; Felippa, C.A. (2000): A variational principle for the formulation of partitioned structural systems. *International Journal for Numerical Methods in Engineering*, Vol 47, pp. 395-418.

Ransom, J.B.; McCleary, S.L.; Aminpour, M.A. (1993): A New Interface Element for Connecting Independently Modeled Substructures. *Proceeding of 34th AIAA/ASME/ASCE/AHS/ASC Structures, Structural Dynamics, and Material Conference*, Paper No. AIAA-93-1503.

Shepard, D. (1968): A two-dimensional function for irregularly spaced data. *Proceeding of ACM National Conference*, pp. 517-524.

